MECHANICAL PROPERTIES OF 17-4PH STAINLESS STEEL AT VARIOUS LASER SINTERING PROCESS PARAMETERS

A. Steponavičiūtė [a], K. Stravinskas [a], A. Selskienė [a], J. Tretjakovas [b],

R. Petkus [a], and G. Mordas [a]

[a] *Center for Physical Sciences and Technology, Savanorių 231, 02300 Vilnius, Lithuania*
[b] *Vilnius Gediminas Technical University, Saulėtekio 11, 10223 Vilnius, Lithuania*
Email: ada.steponaviciute@ftmc.lt

As a material for conventional manufacturing, iron and its alloys had been an object of numerous studies in the past and, as a result, steel became one of the best-known metal alloys in industry. However, new manufacturing technologies, such as additive manufacturing (AM), open new possibilities for the same materials. In this paper, we investigate stainless steel powder for additive manufacturing technologies and parts fabricated from it. Powder chemical composition and morphology are presented in the study. The influence of laser power and laser scanning speed on the mechanical properties of materials and microstructure was studied, and the experimental results showed the optimal energy density values between 50 and 65 J/mm^3. However, the value of energy density varies depending on which parameters are observed, i.e. the optimum energy density value is different for the ultimate tensile stress (UTS) and surface roughness or the Young's modulus and hardness.

Keywords: additive manufacturing, mechanical properties, microstructure, stainless steel, metal powder

1. Introduction

Additive manufacturing (AM) is a manufacturing technology used for 3D object production from materials in the form of powders, liquids and wires. The selected material is added layer upon layer until a 3D object is formed. A wide range of materials can be applied in AM, but metal AM is considered to have the most promising future due to the versatility which metal as a material can offer. Most often the chosen material is metal powder [1, 2]. Each thin layer of metal powder is melted by a laser beam, and the process is followed by rapid solidification. After the solidification, a new powder layer is deposited, and the process is repeated until the fabrication of a fully dense part is completed [3–6]. Metal powder sintering technologies, such as laser metal deposition (LMD), direct metal laser sintering (DMLS) and selective laser melting (SLM), can be used for part fabrication using different metals and their alloys, such as stainless steel, aluminium, titanium, cobalt-chromium alloys, copper, and others [7–11].

Although iron and its alloys have been used in conventional manufacturing for a long time and most of the advantages and disadvantages of these materials are well known, using them in AM to achieve high quality steel can be problematic. The mechanical properties of parts produced via AM are related to the process parameters utilized during the printing process. According to Yadollahi et al. [12], these parameters have a direct influence on the thermal cycle, which is inevitable during the manufacturing process, and therefore, on the microstructure of the manufactured components. The relative density and microstructure of such components influence their mechanical strength under static and cyclic loading.

Researchers have studied how certain parameters, such as laser power, laser scanning speed, layer thickness and build direction, influence mechanical properties and surface quality of additively manufactured stainless steel parts. The results show that big differences in mechanical properties are caused by specimens build direction and layer thickness [13]. However, apart from build direction and layer thickness, the quality of a part is highly dependable on laser process parameters. In fact, according to Liverani et al. [14], laser power has a significantly higher influence on relative density compared to build direction and hatch spacing. In order to determine how various process parameters influence the quality of as-built parts, a physical quantity referred to as energy density is often applied in research works [13, 15, 16]. It has been determined that the microstructure of as-built parts changes significantly according to the applied energy density. The formation of smooth continuous tracks can be achieved under the irradiation of a suitable laser energy density, which depends on the properties of a material. In metal AM processes, porosity can be observed either due to not high enough values of energy density or due to too high values. When the energy density is not high enough, the material does not melt completely. When the energy density is much higher, the evaporation of metals occurs, vapour cavities collapse and cause large voids, also known as keyholes, to form in the alloy [17]. In order to avoid such voids and form low-porosity parts, a high densification rate of alloys is necessary [18]. Yang et al. [19] produced implants with enhanced overall performance for orthopaedic application from a Mg-based composite. The alloy exhibited a great formability with a high densification rate.

The specimens manufactured with the same energy density level acquired by using different laser power and scanning speed values show non-consistent microstructural results with significantly different levels of porosity [20]. It is apparent that energy density as a sole parameter is not an indicator significant enough for the porosity level evaluation of additively manufactured metal parts. The relation between high and low values of laser power and scanning speed may yield different results and cause high porosity levels for different reasons, even though energy density levels remain the same.

Different studies, evaluating mechanical properties of additively manufactured metal parts, already exist; however, such studies have a deeper insight into certain properties such as surface roughness, microstructure or strength and lack thorough understanding of the immediate influence of AM process parameters on various qualitative parameters. Tensile tests and SEM micrographs are required to objectively evaluate the relationship between porosity and mechanical properties of parts additively manufactured using different sets of parameters. The investigation of the relationship between the process parameter and mechanical and microstructural property may result in finding the correlation between an optimal set of parameters and dense parts with promising mechanical properties.

In this work, bone-shape and rectangular specimens were prepared and tested in order to determine the influence of laser scanning speed and laser power on the mechanical properties of LPW 17-4PH stainless steel used in metal AM. The evaluation of ultimate tensile stress (UTS) and yield stress, Young's modulus, hardness, surface roughness and microstructure, as well as detailed material experiments were carried out in this research. The obtained results were summarized, as well as a process parameter zone for optimal mechanical properties (surface roughness, ultimate and yield stress) and microstructure was determined.

2. Materials and methods

2.1. Metal powder

The powder which was examined in the paper was the 17-4PH stainless steel produced by *Carpenter Additive*. It is a martensitic precipitation strengthened stainless steel renowned for a high strength, good mechanical properties and a good corrosion resistance up to 300°C. Moreover, this alloy is the most common member of the class and is generally considered to have the best weldability [21]. However, this powder characterization is not completed (compared with CoCrMo powder, for example [22]), whereas its application in additive technologies still leaves many questions.

2.2. Laser metal sintering and specimen manufacturing

The process of metal powder sintering is applied using a commercial machine EOSINT M280 (*EOS GmbH–Electro Optical Systems*, Krailling, Germany). EOSINT M280 has a 200 W of 1030 nm built-in Yb fibre laser and a high-speed scanner comprising precision galvanometer (11 *μ*rad) with temperature compensation. The F-theta objective focuses a laser beam at a building area in 100 *μ*m. Therein, the powder layer thickness is 40 *μ*m. The manufacturing process takes place in the inert nitrogen atmosphere on the preheated (80°C) building platform.

In our investigations, the specimens were built directly on the base plate with a 2 mm soft support, in the horizontal orientation having an 85 deg angle with the powder scraper moving direction. The specimens were of two types: a) square of 20 × 20 and 10 mm in height; b) bone-shaped ones with 3 mm in width and height, and 35 mm in length (Fig. 1). The first type was used for microstructure studies, whereas the second one was applied for the investigation of mechanical properties. The selected dimensions were a compromise between standard consistency and manufacturing costs. After the building process, the specimens were taken out from the process chamber, cleaned from excessive powder by a vacuum cleaner, and support structures were removed. The produced specimens were heat-treated to reach the H900 condition. To achieve this condition, specimens must be heated at 482°C for 1 h and left to cool to room temperature in the furnace. This heat treatment is usually recommended to achieve the reduction of process-induced tensile residual stresses, with a potential beneficial effect on the tensile response of the built parts [23, 24]. Then, a vertical cross-section cut was made on the square type specimens, which were polished with a Tegramin-25 (*Struers*, Denmark).

In this study, specimen manufacturing was performed using different sintering process parameters. During the first part of the experiment, laser power was changed from 70 to 195 W, with a step of 25 W, while the scanning speed was kept constant (800 mm/s). During the second part of the experiment, the scanning speed ranged from 200 to 1000 mm/s with a step of 200 mm/s, while the laser power value was kept constant (120 W). The hatch spacing and layer thickness chosen for both experiments were 100 and 40 *μ*m, respectively. For scanning strategy, 4 mm stripes with a rotation angle of 67 deg after each layer were applied for all experiments. In order to achieve accurate experimental results, five specimens were manufactured for each set of parameters.
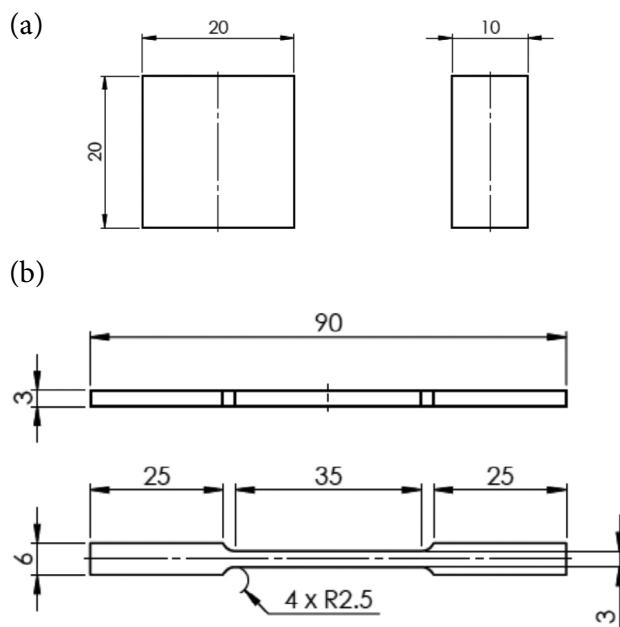
2.3. Characterisation

Scanning electron microscopy (SEM) was applied to study the morphology of alloy profiles and metal powder particles. The used SEM has a dual beam system Helios NanoLab 650 (*FEI Company*) with an energy dispersion X-ray spectrometer INCA-Energy (*Oxford Instruments*). The system is supplied with a Schottky type field emission electron source and a focused Ga ions source. The element mappings were carried out under an accelerating voltage of 8 kV and the beam current of 3.2 nA. The powder particles were deposited on the metal film and then analysed [19]. The element analysis was also carried out by energy dispersive spectrometry (EDS) during SEM observations.

The carbon and sulphur analyser CS-2000 is dedicated to a precise determination of carbon and sulphur. Regardless of which furnace is used in the device, carbon and sulphur in the sample

Fig. 1. Specimens for microstructure studies (a) and tensile tests (b).

110 ISSN 1648-8504 eISSN 2424-3647

A. Steponavičiūtė et al. / Lith. J. Phys. **64**, 107–121 (2024)

form gaseous molecules such as SO_2 and CO_2 during the combustion. The released amounts of CO_2 and SO_2 are measured in up to 4 element-selective infrared cells. The typical sample weight for carbon/sulphur analysis is about 50 to 1000 mg. This is sufficient to reliably detect concentrations from 1 ppm to 100%.

Density measurements were performed using an analytical balance *Radwag* AS 520.R2 PLUS. The density was determined by first weighing the sample in air and then weighing the same sample in water. Since the same sample is weighed in water of a known temperature which has been measured and entered into an analytical balance, the result of density determination is automatically shown on the balance display.

The X-ray diffractometer D8 Advance (*Bruker AXS*, Germany) does a traditional X-ray powder diffraction (XRD) and pair distribution function (PDF) analysis of all sample types (liquids to lose powders, from thin films to solid blocks). The instrument has a 2.4 kW sealed X-ray tube with a Cu anode, the optics of parallel beam/Bragg–Brentano, a V grove Ge monochromator and a scintillation detector. The sample stages are Eulerian cradle (Ψ, φ, x, y, z). The powder diffraction database is PDF2 of the 2003 release.

Each test specimen had the number of defects evaluated by inspecting the combined area of all visible defects (pores, holes) in a cross-section picture of every specimen, which were analysed with an optical microscope OLYMPUS BX51TF (*Olympus*, Germany).

The TIRAtest 2300 (with Real-Time Power-PC controller based on 800 MHz CompactRIO) testing equipment was used to carry out the tensile stress experiments under static loading of bone-shaped specimens by Standard EN ISO 6892–1:2016. The TIRAtest 2300 has a test area of H 1000 × W 550 mm and a maximum test load of 100 kN and the possibility to apply dynamometers of varying force (10 and 100 N, 10 and 100 kN). The system moves in a helical manner and has a speed range of 0.00012–10 mm/s.

Using the TIRAtest 2300 testing equipment, the behaviour of stainless steel can be determined by the non-linear stress σ – strain ε diagram experimentally and evaluated from the tensile testing what is ideal for analysing the material's strength against the maximum stress from being stretched

or pulled before breaking. This test method is used to determine yield stress, UTS, and Young's modulus in this paper.

Hardness tests were carried out using a *Zwick/Roell* ZHU machine. The hardness tester has a test area of H 670 × D 105 mm with no width limitations and can be used for test loads of up to 2.5 kN using Rockwell, Brinell, Vickers or IIT test methods with ball or diamond shaped indenters. The tests were carried out using the Rockwell HRB scale with a 1.588 mm diameter ball-shaped indenter. Three tests were carried out for each specimen.

The surface roughness of the specimens was tested using a Dektak 150 *Veeco* stylus profiler. The profiler has a maximum scan length range of 55 mm and can be used to measure specimens of up to 60 mm in height. The sample stage has a manual X/Y/ θ, 100 × 100 mm X-Y translation, 360° rotation and manual levelling. The specimens were tested using a stylus with a radius of 5 μm, the applied stylus force was 1 mg and the scan speed was 0.33 mm/s.

3. Results and discussion

3.1. *Powder morphology and chemical composition*

The manufacturer *LPW Technology Ltd.* states that the size of powder particles is around 15–45 μm. Our high-resolution images of the metal particle collection of the said powder are presented in Fig. 2. The selected scale bar represents 200, 100, 50 and 10 μm. The images show that LPW 17-4PH has a polydisperse particle size distribution from 15 to 45 μm. Most of the particles seem quite spherical and have a smooth surface. Particles which have a different, less spherical shape and various attachments might be a result of smaller spherical particles sticking to larger particles. The sticking of smaller particles causes the formation of agglomerates of a slightly rougher shape. Wherein, the maximum agglomerate size is about 45 μm. The maximum size is limited due to the powder production process when particles are collected and brushed through a 45 μm sieve. The size of the smallest particles is determined by the diameter of the atomiser jet nozzle applied for metal powder production [25]. In our study, particles as small as 15 μm were observed.

The chemical composition of the powder provided by the manufacturer *Carpenter Additive*

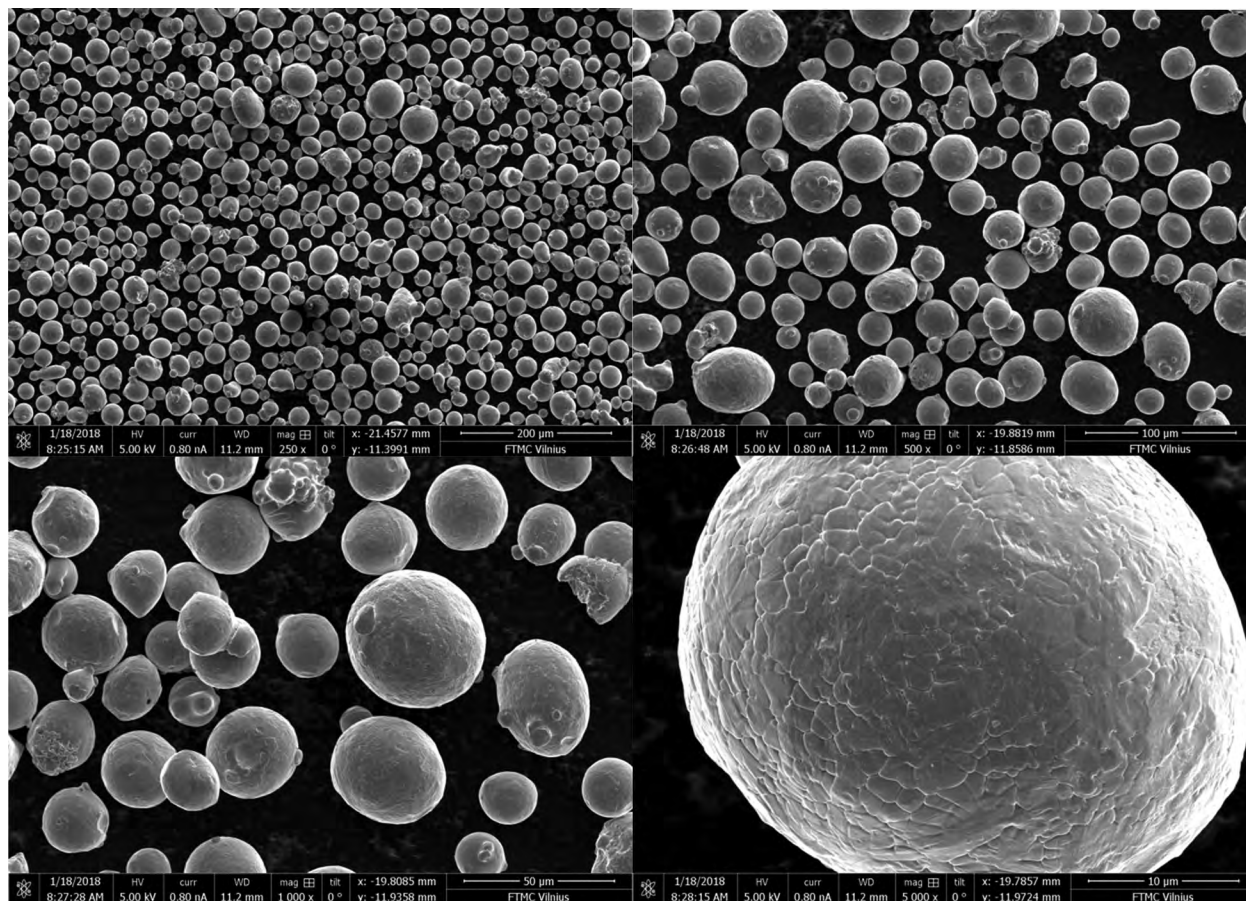Fig. 2. SEM micrographs of the 17-4PH powder (200, 100, 50 and 10 μm scales).

(at.%) [21] is listed in Table 1 as the default chemical composition. The default chemical composition is similar to the one regulated by the ASTM standard for the 17-4PH stainless-steel [26] and has only a slightly higher maximum concentration of carbon (<0.10 at.% compared with <0.07 at.%). Moreover, the default chemical composition from the manufacturer provides the concentration of tantalum list-ed together with niobium, whereas tantalum is not apparent in the chemical composition of the ASTM standard. The results of SEM-EDS analysis of 10 individual particles showed that the elemental composition corresponded to the individual chemical element ranges listed by the powder manufacturer. The results of carbon and sulphur analysis show that carbon and sulphur concentrations are within

Table 1. Chemical composition (at.%) of the 17-4PH powder.

Element	Fe	Cr	Ni	Cu	Mn	Si	Mo	Nb+Ta	Nb	S	P	S
ASTM Standard	balance	15.0–17.0	3.0–5.0	3.0–5.0	<1.0	<1.0	–	–	0.15–0.45	<0.070	<0.040	<0.030
Default	balance	15.0–17.0	3.0–5.0	3.0–5.0	<1.0	<1.0	<1.0	0.2–0.5	–	<0.010	<0.040	<0.030
SEM-EDS (our study)	73.8	16.0	4.6	4.2	0.65	0.77	–	–	–	–	–	–
Carbon/ sulphur analyser (our study)	–	–	–	–	–	–	–	–	–	0.06	–	0.01

the range of the ASTM standard (0.06 at.% C and 0.01 at.% S). The concentration (at.%) of all chemical elements complies with the ASTM standard regulations and is in the range of the chemical composition provided by the powder manufacturer.

3.2. Alloy elemental distribution and structure

Using the investigated 17-4PH powder, an alloy sample was produced by applying the following laser power and scanning speed: 195 W, 800 mm/s. SEM-EDS mapping (Fig. 3) was performed to support the distribution of various elements in the manufactured sample. The distribution of various elements is even and the tested sample has the following chemical composition: 73.8±0.09 at.% of Fe, 15.96±0.03 at.% of Cr, 4.53±0.03 at.% Ni, 4.28±0.08 at.% Cu, 0.77±0.02 at.% Si, and 0.41±0.04 at.% of Mn.

Figure 4 shows the XRD pattern of the 17-4PH alloy. It was determined that the highest inten-sity XRD peak corresponds to the chromium-iron phase $Cr_{0.5}Fe_{0.5}$ (ICDD card #04-003-4099). The lowest intensity peak is attributable to the chromium–iron–carbon phase $CrFe_7C_{0.45}$ (ISDD card #04-009-1699). The alloy $Cr_{0.5}Fe_{0.5}$ has a cubic body centred structure, and the carbide $CrFe_7C_{0.45}$ has a cubic face centred structure. There is no peak, which could be attributed to the austenite phase (ICDD card #00-052-0513). Similar results were obtained by Sabooni et al. [27] where the use of LPW 17-4PH powder resulted in alloy with the for-mation of a ferritic structure and a very low (<2%) amount of austenite was observed while applying different aging times from 0.5 to 24 h.

3.3. Alloy microstructure

Laser energy density is a key factor affecting the mechanical properties of parts fabricated by DMLS. The most widely used volume energy density
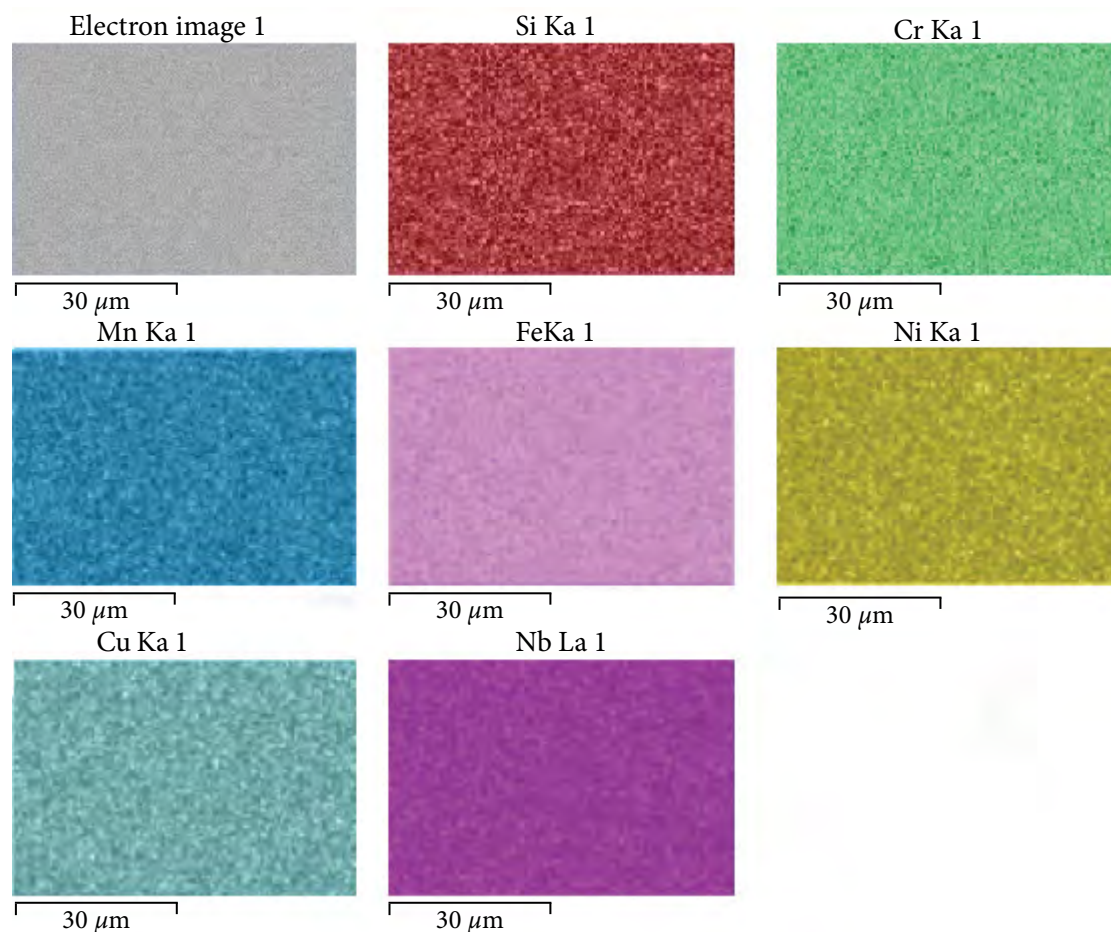

Fig. 3. SEM-EDS mapping of a sample printed with a laser scanning speed of 800 m/s and a laser power of 195 W.
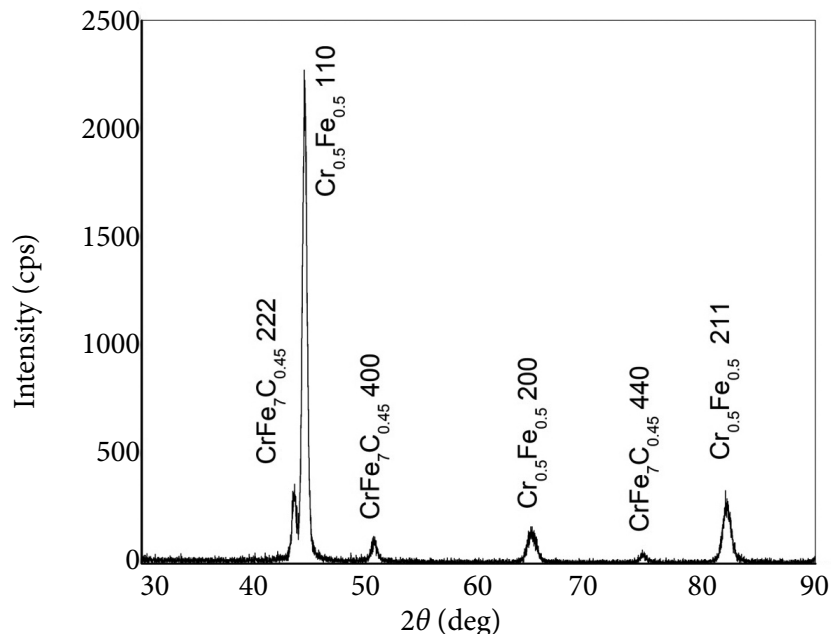
Fig. 4. XRD pattern of the 17-4PH alloy.

E (J/mm³) is defined in Eq. 1, where *P* is the power (W), *v* is the scanning speed (mm/s), *h* is the hatch spacing (mm), and *t* is the layer thickness (mm) [28]. Hatching spacing and layer thickness values were kept constant throughout the experiment and were 100 and 40 *μ*m, respectively:

$$E = \frac{P}{v \cdot h \cdot t}. \tag{1}$$

The influence of volumetric energy density on alloy microstructure and relative density was determined experimentally. We classified the cross-sectional micrographs by attributing them to four different energy density ranges: 20–35 J/mm³ (I), 35–50 J/mm³ (II), 50–65 J/mm³ (III) and 65–80 J/mm³ (IV). A visible decrease in the amount of defects (pores) can be observed when the energy density is increased, as shown in Fig. 5. All the defects
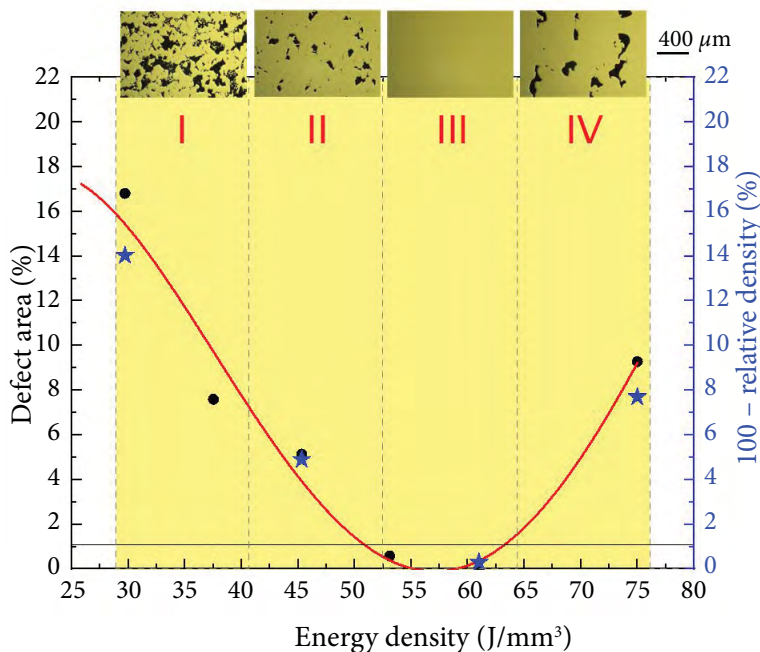

Fig. 5. Microstructural evolution of additively manufactured parts.

compiled take up 16.5–17.5% of the area in I, 5–7% in II and less than 0.5% in III. With further increase of energy density the percentage of defects tends to increase as well and takes up about 9% in IV. Wherein, with the increase of energy density, the relative density increases as well and reaches the maximum value of 99.7% (at 61 J/mm³). After this point, the relative density decreases with further increase of energy density. To show a direct correlation between the calculated defect area and the measured relative density, an inverted parameter (100 – relative density, %) is used in Fig. 5.

3.4. Tensile behaviour

The specimens were 3D printed using different scan speed and laser power values, and their mechanical properties, such as ultimate and yield stresses, Young's modulus, and hardness, were tested.

According to Alsalla et al. [10], the microstructure and mechanical properties of specimens change depending on different build directions due to the layer-by-layer production process used in AM. Their study shows that specimens built in a vertical direction have a lower performance compared to specimens build in a horizontal direction. In order to

focus on the process parameters like laser scanning speed and laser power and to eliminate the influence of the build direction on the mechanical properties, all specimens were built in horizontal direction in this study.

As can be seen from the graphs in Fig. 6, the values of yield stress and UTS increase gradually with the increase of laser power when the scanning speed is constant (800 mm/s). The UTS of the sample part printed with the highest laser power is more than four times greater compared to the lowest laser power used in the experiment, yield stress has an increase of a similar size – also more than four times. A gradual growth of Young's modulus is visible. The Young's modulus of the sample part printed with the highest laser power (1250 GPa, 195 W) is more than 3 times greater compared to the lowest laser power (286 GPa, 70 W) used in the experiment.

Figure 7 shows the results obtained with a constant laser power of 120 W and a variable scanning speed. The experiment resulted in consistent analytical data, where the yield stress values decreased gradually when the scan speed was increased. The yield stress difference between the lowest and the highest scanning speed is approximately two times. Young's modulus tends to decrease when
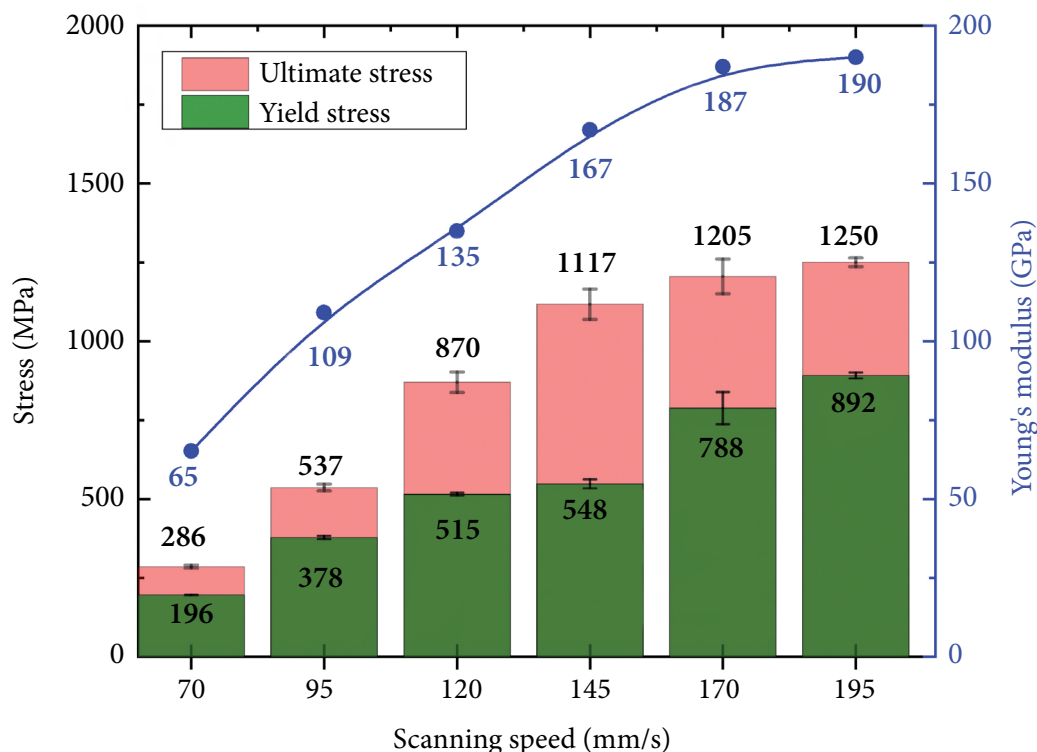

Fig. 6. Mechanical properties of parts printed with a constant scanning speed (800 mm/s).
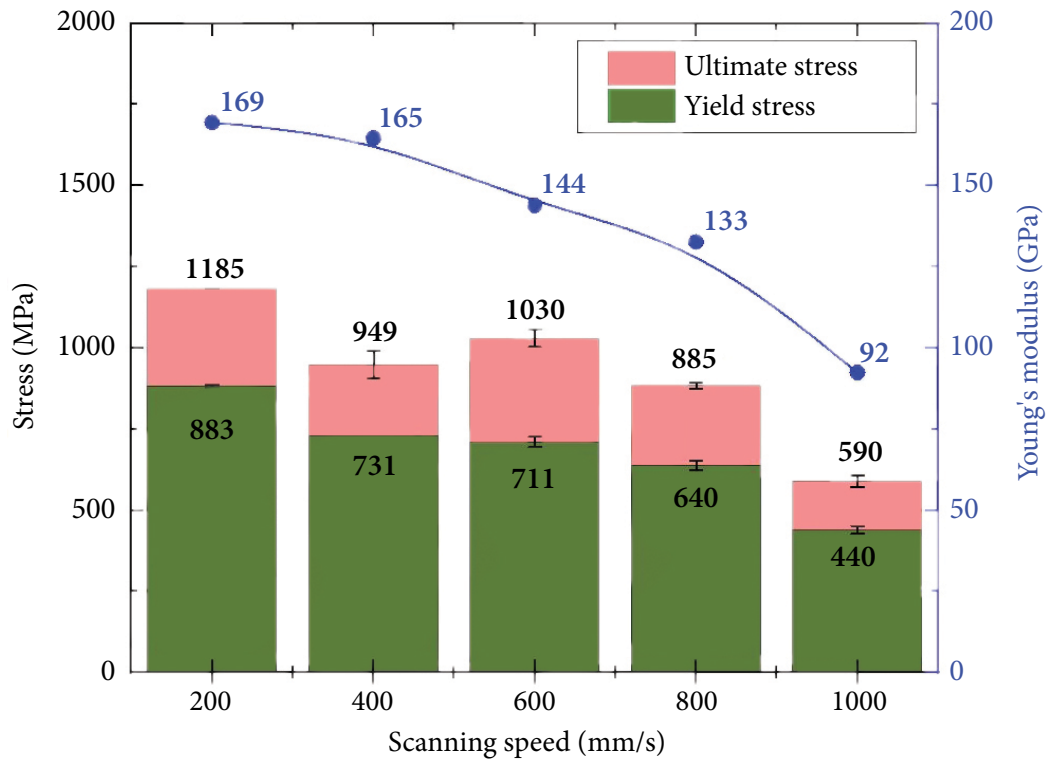
Fig. 7. Mechanical properties of parts printed with a constant laser power.

the scan speed increases and changes from 169 GPa at 200 mm/s to 92 GPa at 1000 mm/s.

During the tensile process, the specimen undergoes a large plastic deformation, and the micro-cavities appear at various imperfections, such as unmolten particles or pores. Large stresses caused by these cavities lead to even more micro-cavities. Eventually, the cavities conjoin together, and the fast-growing tears cause the fracture [29]. Figure 8 shows the tensile fracture surfaces of specimens produced
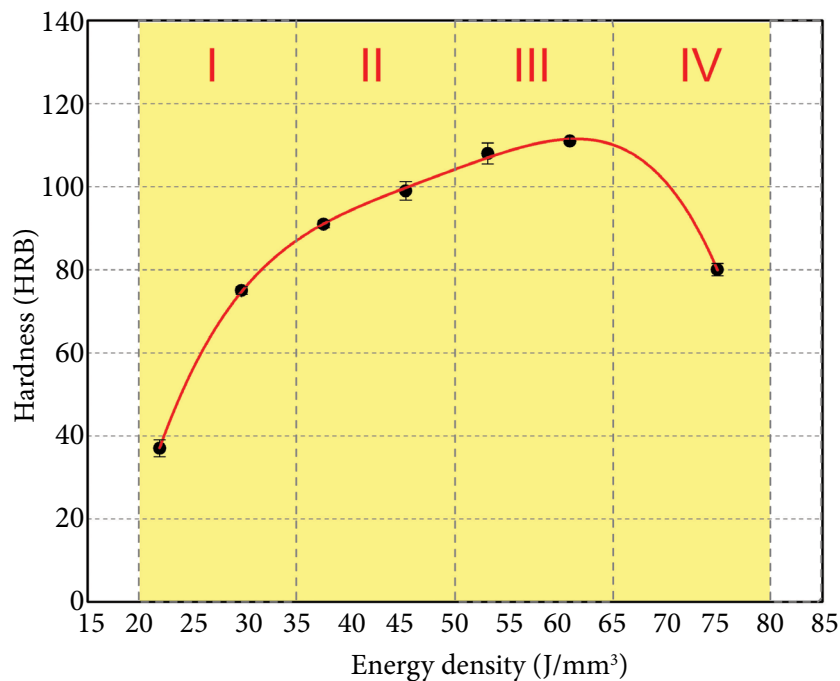
Fig. 8. Fracture morphology.

with different energy density values. Unmolten particles can be observed in the first picture (37.5 J/mm³), which are the result of a relatively low energy density used for the test specimen production. The energy density was not high enough to form a solid alloy and the remaining pores with the unmolten particles resulted in a fast conjoining of micro-cavities, causing a fracture and a relatively low tensile stress. With the increase of energy density, the fracture surface becomes smoother and the unmolten particles are no longer visible in the fractography. No more unmolten particles are visible when the energy density reaches 50.0 J/mm³; however, cleavage fractures and shallow and limited dimples become present, meaning that the plastic deformation is insufficient, and the main fracture mode is a brittle fracture [29]. Small dimples observed in the specimen produced with the energy density value of 61.0 J/mm³ integrate ductile and brittle fractures and result in the highest UTS value throughout the experiment (1250 MPa).

3.5. Hardness and surface roughness

The graph in Fig. 9 shows the hardness (Rockwell HRB scale) of the parts printed using different energy density values. The values are divided into four sections: 20–35 J/mm³ (I), 35–50 J/mm³ (II), 50–65 J/mm³ (III) and 65–80 J/mm³ (IV). The increase in hardness can be seen in the first three sections up to the energy density of 61 J/mm³, where the hardness is 111.0±0.2 HRB. With a higher energy density in section IV, the hardness starts decreasing and is 80.0±1.5 HRB at 75 J/mm³. The best surface roughness is achieved in section III, so the optimal energy density window

for the best hardness results is the one between the values of 50–65 J/mm³, respectively.

The SEM micrographs of the surface of specimens processed using different energy density values are presented in Fig. 10. The micrograph on the left shows the surface of a specimen with a volume energy density of 20 J/mm³. Due to a low energy density the melting process is not complete. As a result, a rough, uneven surface with the 21.1±9.9 μm roughness and unmolten particles sticking to it can be observed. The micrograph in the middle (energy density 51 J/mm³) shows a much smoother surface with hatch lines visible. The used energy density was enough to completely melt the powder particles, and a surface roughness of 15.6±1.4 μm is achieved. The micrograph on the right was printed using a set of parameters with an energy density of 71 J/mm³. Bigger bump-like structures are visible, causing the surface roughness R_a value to jump to 34.6±2.0 μm.

The graph in Fig. 11 shows the surface roughness R_a for the specimens produced using different energy density values. As seen in the graph, the R_a values vary from 8 to 28 μm, whereas the lowest surface roughness is achieved when the energy density is 53 J/mm³. It can be seen from Eq. (1) that by increasing the laser power and/or decreasing the scanning speed, the energy density increases as well, resulting in higher temperature. Choosing a low laser scanning speed can improve surface roughness because there is more time for the so-called melt pools (areas of molten metal powder) to flatten before they solidify. However, if the selected speed is too slow, melt pools can become wider and increase in volume. This causes a higher thermal difference and a higher variation of surface tensions across the molten area.

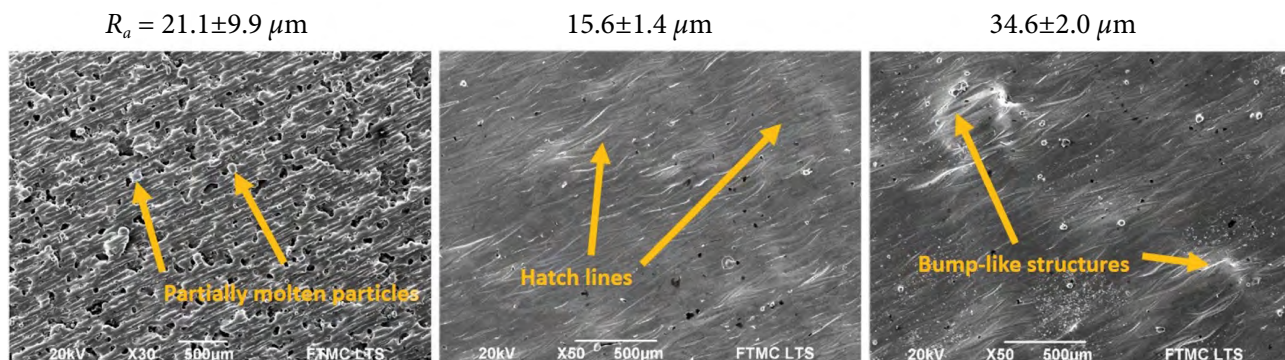R_a = 21.1±9.9 μm   15.6±1.4 μm   34.6±2.0 μm

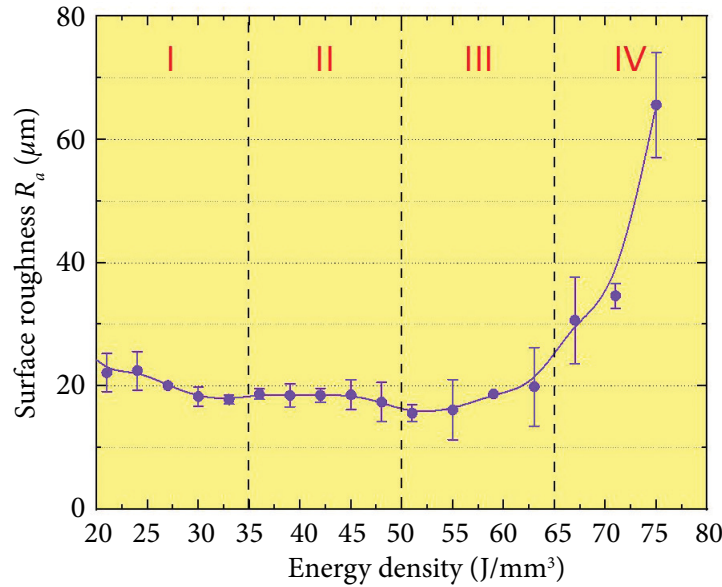Fig. 9. Hardness of parts printed using different energy density values.

Fig. 10. Surface roughness of specimens produced with energy density values of 20 J/mm^3 (left), 51 J/mm^3 (middle) and 71 J/mm^3 (right).

In order to reduce thermal differences and surface tension, 'balling' might occur, i.e. a melt pool might break into smaller entities and cause a poor surface roughness [30]. On the other hand, if the scanning speed is too high, metal powder particles do not melt completely and unmolten particles stick to the molten surface, causing a poor surface quality.

3.6. *Summary and comparison of the results*

During this study, the influence of energy density on various mechanical properties of specimens additively manufactured from the 17-4PH stainless-steel powder was investigated. The results showed that the energy density range of 50–65 J/mm^3 (III) lead to the best mechanical properties of produced parts. The porosity and relative density in this energy density range were <0.5% and 99.7±0.1%, respectively. Other researchers achieved the relative density of 96.6±0.5% in the same energy density range [31]. The same paper states the hardness value of 103.5±1.5 HRB, whereas the hardness determined in our study is 111.0±0.2 HRB. UTS and yield strength values in the 50–65 J/mm^3 range in our study are 1250±14 and 892±9 MPa, respectively [32]. They achieved similar results in their work, where the UTS value was 1240±50 MPa and the yield stress was 910±80 MPa. The lowest surface roughness R_a in our study is 15.6±1.4 μm.
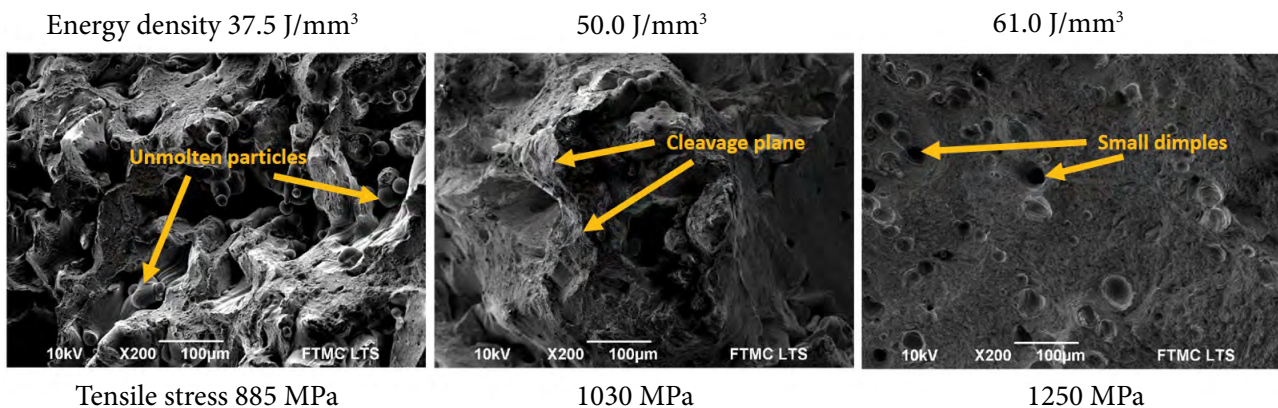

Fig. 11. Surface roughness of specimens printed with different energy density values.

Table 2. Mechanical properties of heat-treated specimens.

Parameter	Additively manufactured	ASTM A564 standard [26]
Relative density, %	99.7±0.1	100
Porosity, %	<0.5	0
Young's modulus, GPa	190.0±1.6	200
Yield stress, MPa	892±9	1170
Ultimate tensile stress, MPa	1250±14	1310
Hardness, HRB	111.0±0.2	113
Surface roughness R_a, μm	15.6±1.4	–

This value is similar to other researchers' results, where the R_a value is around 12.94–15.92 μm [33]. The maximum value of the Young's modulus in this paper is 190.0±1.6 GPa. That parameter was not evaluated by other authors in the described energy density range for the 17-4PH stainless-steel; however, according to the ASTM standard, the achieved value of Young's modulus is similar to the one of a wrought material (200 GPa, Table 2).

The mechanical properties of additively manufactured 17-4PH stainless-steel specimens were compared to those of a wrought stainless-steel of the same grade. Both materials were heat-treated to the H900 condition. As can be seen from Table 2, the results obtained through AM are similar to the ASTM A564 standard [26] for a wrought material. The close comparison proves that additively manufactured 17-4PH stainless steel parts can achieve a commercially available product level and can show a great potential for a wide variety of engineering applications.

4. Conclusions

1. The SEM analysis demonstrates that the inspected powder has a polydisperse particle size distribution of 10–50 μm. According to the SEM-EDS results of 10 powder particles, the powder consists of 73.8 at.% of Fe, 16.0 at.% Cr, 4.6 at.% Ni, 4.2 at.% Cu, 0.77 at.% Si and 0.65 at.% of Mn, whereas the determined chemical composition corresponds to the default chemical composition provided by the manufacturer.

2. The SEM-EDS elemental mapping of a sample alloy has been performed and the obtained results correspond to the SEM-EDS results of the powder. The XRD patterns of the alloy show that the highest intensity XRD peak is attributable to the chromium–iron phase $Cr_{0.5}Fe_{0.5}$ and the lowest intensity peak matches the chromium–iron–carbon phase $CrFe_7C_{0.45}$.

3. Depending on the cross-sectional microstructure of produced specimens, four energy density ranges were determined for an easier classification of the samples: 20–35 J/mm³ (I), 35–50 J/mm³ (II), 50–65 J/mm³ (III) and 65–80 J/mm³ (IV). Each of them has significant differences in porosity and relative density. The evolution of porosity and relative density correspond to other mechanical properties, studied in this paper. Surface roughness R_a values vary from 15.6 to 68.3 μm depending on the energy density values. The lowest surface roughness is achieved when the energy density is 53 J/mm³. An increase in hardness can be seen from 38 HRB at the energy density 22 J/mm³ up to 111 HRB at 61 J/mm³.

4. UTS and yield stress values have been obtained from the specimens produced with different laser scanning speed and laser power values. With a constant laser power (120 W) and an increasing scanning speed (from 200 to 1000 mm/s), a decrease in UTS, yield stress, and Young's modulus is observed. With a constant laser scanning speed (800 mm/s) and the increase of laser power (from 70 to 195 W), UTS and yield stress and Young's modulus values increase.

5. The best mechanical properties of the 17-4PH alloy were achieved in the energy density range of 50–65 J/mm³ (III): porosity and relative density <0.5% and 99.7%, respectively, surface roughness R_a 15.6 μm, hardness 111 HRB, UTS 1250 MPa, yield stress 892 MPa, and Young's modulus 190 GPa.

119 ISSN 1648-8504 eISSN 2424-3647

A. Steponavičiūtė et al. / Lith. J. Phys. **64**, *107–121 (2024)*

References

[1] E. Chlebus, B. Kuźnicka, T. Kurzynowski, and B. Dybała, Microstructure and mechanical behaviour of Ti–6Al–7Nb alloy produced by selective laser melting, Mater. Charact. **62**(5), 488–495 (2011), https://doi.org/10.1016/J.MATCHAR.2011.03.006

[2] I. Yadroitsev, A. Gusarov, I. Yadroitsava, and I. Smurov, Single track formation in selective laser melting of metal powders, J. Mater. Process. Technol. **210**(12), 1624–1631 (2010), https://doi.org/10.1016/J.JMATPROTEC.2010.05.010

[3] J.P. Kruth, P. Mercelis, J. Van Vaerenbergh, L. Froyen, and M. Rombouts, Binding mechanisms in selective laser sintering and selective laser melting, Rapid Prototyp. J. **11**(1), 26–36 (2005), https://doi.org/10.1108/13552540510573365

[4] D.D. Gu, W. Meiners, K. Wissenbach, and R. Poprawe, Laser additive manufacturing of metallic components: Materials, processes and mechanisms, Int. Mater. Rev. **57**(3), 133–164 (2012), https://doi.org/10.1179/1743280411Y.0000000014

[5] *Springer Handbook of Mechanical Engineering*, eds. K.-H. Grote and E.K. Antonsson (Springer, 2009).

[6] L.E. Murr, S.M. Gaytan, D.A. Ramirez, E. Martinez, J. Hernandez, K.N. Amato, P.W. Shindo, F.R. Medina, and R.B. Wicker, Metal fabrication by additive manufacturing using laser and electron beam melting technologies, J. Mater. Sci. Technol. **28**(1), 1–14 (2012), https://doi.org/10.1016/S1005-0302(12)60016-4

[7] Y. Tang, H.T. Loh, Y.S. Wong, J.Y.H. Fuh, L. Lu, and X. Wang, Direct laser sintering of a copper-based alloy for creating three-dimensional metal parts, J. Mater. Process. Technol. **140**(1–3), 368–372 (2003), https://doi.org/10.1016/S0924-0136(03)00766-0

[8] G.A. Ravi, X.J. Hao, N. Wain, X. Wu, and M.M. Attallah, Direct laser fabrication of three dimensional components using SC420 stainless steel, Mater. Des. **47**, 731–736 (2013), https://doi.org/10.1016/j.matdes.2012.12.062

[9] C. Yan, L. Hao, A. Hussein, P. Young, J. Huang, and W. Zhu, Microstructure and mechanical properties of aluminium alloy cellular lattice structures manufactured by direct metal laser sintering, Mater. Sci. Eng. A **628**, 238–246 (2015), https://doi.org/10.1016/j.msea.2015.01.063

[10] H.H. Alsalla, C. Smith, and L. Hao, The effect of different build orientations on the consolidation, tensile and fracture toughness properties of direct metal laser sintering Ti-6Al-4V, Rapid Prototyp. J. **24**(2), 276–284 (2018), https://doi.org/10.1108/RPJ-04-2016-0067

[11] A. Barazanchi, K. Li, B. Al-Amleh, K. Lyons, and J. Waddell, Mechanical properties of laser-sintered 3D-printed cobalt chromium and soft-milled cobalt chromium, Prosthesis **2**(4), 313–320 (2020), https://doi.org/10.3390/prosthesis2040028

[12] A. Yadollahi, N. Shamsaei, S.M. Thompson, and D.W. Seely, Effects of process time interval and heat treatment on the mechanical and microstructural properties of direct laser deposited 316L stainless steel, Mater. Sci. Eng. A **644**, 171–183 (2015), https://doi.org/10.1016/j.msea.2015.07.056

[13] J. Delgado, J. Ciurana, and C.A. Rodríguez, Influence of process parameters on part quality and mechanical properties for DMLS and SLM with iron-based materials, Int. J. Adv. Manuf. Technol. **60**(5–8), 601–610 (2012), https://doi.org/10.1007/s00170-011-3643-5

[14] E. Liverani, S. Toschi, L. Ceschini, and A. Fortunato, Effect of selective laser melting (SLM) process parameters on microstructure and mechanical properties of 316L austenitic stainless steel, J. Mater. Process. Technol. **249**, 255–263 (2017), https://doi.org/10.1016/j.jmatprotec.2017.05.042

[15] L. Thijs, F. Verhaeghe, T. Craeghs, J. Van Humbeeck, and J.P. Kruth, A study of the microstructural evolution during selective laser melting of Ti-6Al-4V, Acta Mater. **58**(9), 3303–3312 (2010), https://doi.org/10.1016/j.actamat.2010.02.004

[16] J.H. Yi, J.W. Kang, T.J. Wang, X. Wang, Y.Y. Hu, T. Feng, Y.L. Feng, and P.Y. Wu, Effect of laser energy density on the microstructure, mechanical properties, and deformation of Inconel 718 samples fabricated by selective laser melting, J. Alloys Compd. **786**, 481–488 (2019), https://doi.org/10.1016/j.jallcom.2019.01.377

[17] J.D. Madison and L.K. Aagesen, Quantitative characterization of porosity in laser welds of stainless steel, Scr. Mater. **67**(9), 783–786 (2012), https://doi.org/10.1016/j.scriptamat.2012.06.015

[18] M. Guo, D. Gu, L. Xi, L. Du, H. Zhang, and J. Zhang, Formation of scanning tracks during selective laser melting (SLM) of pure tungsten powder: Morphology, geometric features and forming mechanisms, Int. J. Refr. Met. Hard Mater. **79**, 37–46 (2019), https://doi.org/10.1016/j.ijrmhm.2018.11.003

[19] Y. Yang, C. Lu, L. Shen, Z. Zhao, S. Peng, and C. Shuai, In-situ deposition of apatite layer to protect Mg-based composite fabricated via laser additive manufacturing, J. Magn. Alloy. **11**(2), 629–640 (2021), https://doi.org/10.1016/j.jma.2021.04.009

[20] H. Gu, H. Gong, D. Pal, K. Rafi, T. Starr, and B. Stucker, Influences of energy density on porosity and microstructure of selective laser melted 17-4PH stainless steel, in: *Proceedings of the 24th Annual International Solid Freeform Fabrication Symposium* (2013) pp. 474–489.

[21] *PowderRange 17-4PH Datasheet*, Vol. 4548 (2000).

[22] G. Mordas, V. Jasulaitienė, A. Steponavičiūtė, M. Gaspariūnas, R. Petkevič, A. Selskienė, R. Juškėnas, D.F. Paul, J.E. Mann, V. Remeikis, and G. Račiukaitis, Characterisation of CoCrMo powder for additive manufacturing, Int. J. Adv. Manuf. Technol. **111**(11–12), 3083–3093 (2020), https://doi.org/10.1007/s00170-020-06236-3

[23] C. Sanz and V. García Navas, Structural integrity of direct metal laser sintered parts subjected to thermal and finishing treatments, J. Mater. Process. Technol. **213**(12), 2126–2136 (2013), https://doi.org/10.1016/j.jmatprotec.2013.06.013

[24] N.T. Aboulkhair, I. Maskery, C. Tuck, I. Ashcroft, and N.M. Everitt, Improving the fatigue behaviour of a selectively laser melted aluminium alloy: Influence of heat treatment and surface quality, Mater. Des. **104**, 174–182 (2016), https://doi.org/10.1016/j.matdes.2016.05.041

[25] J.J. Dunkley, *ASM Handbook: Powder Metalurgy*, Vol. 7, eds. P. Samal and J. Newkirk (ASM International, 2015).

[26] *17-4PH, 1.4542, X5CRNICUNB16-4 - Stainless steel* (2021), https://virgamet.com/17-4ph-x5crnicunb164-aisi-630-uns-s17400-1-4542-stainless-steel

[27] S. Sabooni, A. Chabok, S.C. Feng, H. Blaauw, T.C. Pijper, H.J. Yang, and Y.T. Pei, Laser powder bed fusion of 17-4 PH stainless steel: A comparative study on the effect of heat treatment on the microstructure evolution and mechanical properties, Addit. Manuf. **46**, 102176 (2021), https://doi.org/10.1016/j.addma.2021.102176

[28] Y. Shang, Y. Yuan, Y. Zhang, D. Li, and Y. Li, Investigation into effects of scanning speed on *in vitro* biocompatibility of selective laser melted 316L stainless steel parts, MATEC Web Conf. **95**, 0–3 (2017), https://doi.org/10.1051/matecconf/20179501009

[29] C. Tan, K. Zhou, W. Ma, P. Zhang, M. Liu, and T. Kuang, Microstructural evolution, nanoprecipitation behavior and mechanical properties of selective laser melted high-performance grade 300 maraging steel, Mater. Des. **134**, 23–34 (2017), https://doi.org/10.1016/j.matdes.2017.08.026

[30] D. Gu and Y. Shen, Balling phenomena in direct laser sintering of stainless steel powder: metallurgical mechanisms and control methods, Mater. Design **30**(8), 2903–2910 (2009), https://doi.org/10.1016/j.matdes.2009.01.013

[31] H. Irrinki, J.S.D. Jangam, S. Pasebani, S. Badwe, J. Stitzel, K. Kate, O. Gulsoy, and S.V. Atre, Effects of particle characteristics on the microstructure and mechanical properties of 17-4 PH stainless steel fabricated by laser-powder bed fusion, Powder Technol. **331**, 192–203 (2018), https://doi.org/10.1016/j.powtec.2018.03.025

[32] M. Mahmoudy, A. Elwany, A. Yadollahi, S.M. Thompson, L. Bian, and N. Shamsaei, Mechanical properties and microstructural characterization of selective laser melted 17-4 PH stainless steel, Rapid Prototyp. J. **23**(2), 280–294 (2017), https://doi.org/10.1108/RPJ-12-2015-0192

[33] K.T. Yang, M.K. Kim, D. Kim, and J. Suhr, Investigation of laser powder bed fusion manufacturing and post-processing for surface quality of as-built 17-4PH stainless steel, Surf. Coatings Technol. **422**, 127492 (2021), https://doi.org/10.1016/j.surfcoat.2021.127492

17-4PH NERŪDIJANČIOJO PLIENO MECHANINĖS SAVYBĖS ESANT ĮVAIRIEMS SUKEPINIMO LAZERIU PROCESO PARAMETRAMS

A. Steponavičiūtė [a], K. Stravinskas [a], A. Selskienė [a], J. Tretjakovas [b], R. Petkus [a], G. Mordas [a]

[a] *Fizinių ir technologijos mokslų centras, Vilnius, Lietuva*
[b] *Vilniaus Gedimino technikos universitetas, Vilnius, Lietuva*

Santrauka

Praeityje geležis ir jos lydiniai, kaip įprastinės gamybinės medžiagos, buvo daugelio tyrimų objektas, dėl to plienas tapo vienu geriausiai žinomų metalo lydinių pramonėje. Tačiau naujos technologijos, tokios kaip adityvioji gamyba, atveria naujas galimybes naudoti tokias pačias medžiagas. Šiame straipsnyje nagrinėjama nerūdijančio plieno milteliai, skirti adityviosios gamybos technologijoms, ir iš jų pagamintos detalės. Tyrime pateikiama miltelių cheminė sudėtis ir morfologija. Buvo ištirta lazerio galios ir skenavimo greičio įtaka medžiagų mechaninėms savybėms ir mikrostruktūrai, o eksperimentiniai rezultatai parodė, kad optimalus energijos tankis yra 50–65 J/mm³. Tačiau energijos tankio vertė skiriasi priklausomai nuo to, kokie parametrai stebimi, t. y. optimali energijos tankio vertė skiriasi, pavyzdžiui, stiprumo ribos ir paviršiaus šiurkštumo arba Jungo modulio ir kietumo atveju.